MICROBEAM SYNCHROTRON RADIATION DIFFRACTION AND FLUORESCENCE STUDY OF OXIDE LAYERS FORMED ON 9Cr ODS STEEL IN SUPERCRITICAL WATER

Arthur T. Motta[1], Andrew D. Siwy[1], Jamie M. Kunkle[1], Jeremy B. Bischoff[1], Robert J. Comstock[2], Yun Chen[3], Todd R. Allen[3].

[1]Department of Mechanical and Nuclear Engineering, 227 Reber Bldg., Penn State University, University Park PA 16802, United States.
[2]Science and Technology Dept., Westinghouse Electric Co. Pittsburgh PA. United States.
[3]Department of Engineering Physics, University of Wisconsin, 3335 Engineering Hall, 1415 Engineering Drive, Madison, WI 53706, United States.

Abstract

Uniform corrosion is a major concern for ferritic-martensitic steels when considered as candidate materials for the supercritical water reactor (SCWR). The corrosion rate depends on alloy composition and microstructure. The corrosion rate depends on alloy composition and microstructure. The best ferritic-martensitic alloys resist corrosion by developing a protective oxide layer that stabilizes oxide growth. To better understand the protection and stabilization mechanism, the structure of oxide layers formed on ferritic-martensitic alloys in supercritical water is studied using both transmission electron microscopy and microbeam synchrotron radiation diffraction and fluorescence. Using the microbeam it is possible to determine phases present using x-ray diffraction and chemical composition using x-ray fluorescence, both as a function of location in the oxide layer. The detailed study of phases present and elemental segregation at interfaces is presented for an oxide formed on 9Cr ODS steel after exposure to supercritical water for 667 hours. In the diffusion layer, both metal and oxide peaks are seen indicating a coexistence of the two phases in the diffusion layer. In the Cr-rich inner layer, a mixture of spinel phase $FeCr_2O4$ and Fe_3O_4 is observed, while in the outer oxide layer, Fe_3O_4 is the predominant phase. Evidence for additional Cr-rich phases near the interfaces is also shown.

1. Introduction

Supercritical water (SCW) is being examined as a coolant for the next generation nuclear reactors because it can provide higher thermal efficiency and plant simplification as compared to current light water reactors. However, corrosion has been identified as a critical materials issue because of the oxidative nature of SCW. In this regard, corrosion resistance becomes one of the key requirements for candidate structural materials to be used in the proposed SCW nuclear reactors [1].

Ferritic/martensitic (F/M) steels offer many advantages as candidate structural material for advanced nuclear energy systems including good swelling resistance, low thermal expansion coefficients, and high thermal conductivity [2]. However, the application of F/M steels is limited due to the quick loss of creep strength when operating temperatures are over ~600°C. One promising approach to achieve higher creep strength at higher temperatures and radiation

damage resistance is to add a fine dispersion of oxide particles in the matrix of the F/M steel[3-5]. The addition of the dispersion particles containing rare earth elements such as Y (in the form of Y_2O_3 oxide particles) has been shown to significantly influence both oxide growth kinetics and adhesion in Fe-base and Ni-base alloys at elevated temperatures, although no generally accepted mechanism exists [6-11].

It is clear that the adhesion of the oxide scale and the overall corrosion kinetics are controlled by the microstructure of the oxide layer. In a recent transmission electron microscopy (TEM) study [11] , such microstructure has been shown to be quite complex and to consist of several sub-layers. Microbeam synchrotron radiation diffraction and fluorescence has been recently used to characterize in detail the oxide layers formed in zirconium alloys, both during corrosion in 360ºC water [12, 13] and during corrosion in high temperature supercritical water and steam [14, 15]. The results gave insights into the different corrosion protection mechanisms between different zirconium alloys.

The purpose of this paper is to report on the application of microbeam synchrotron radiation diffraction and fluorescence and transmission electron microscopy techniques to the characterization of oxide layers formed on 9Cr ODS steel.

2. Experimental Methods

Bar stock of 9Cr ODS ferritic steel (24 mm diameter and 60 mm length) was supplied for this study by the Japan Atomic Energy Agency. The alloy had been annealed at 1050ºC for 60 min, air-cooled, and subsequently tempered at 800ºC for 60 min. The chemical composition of the steel is shown in Table 1. The details of the manufacturing process are described elsewhere [4].

Table 1 Chemical compositions of 9Cr ODS F/M steel (wt%, Bal. Fe)

Alloy	C	O	Si	P	S	Ti	Cr	Mn	Ni	Y	W
9Cr ODS	.14	.14	.048	<.05	.003	.21	8.6	.05	.06	.28	2

The corrosion experiments were performed in a natural circulation supercritical water corrosion loop at 600ºC and 25 MPa with an inlet dissolved oxygen concentration of ~50 ppb. The detailed construction and system capabilities of this supercritical water loop have been described in a previous paper [16]. The exposure duration for the sample examined was 667 h. A scanning electron microscope (SEM) micrograph of the oxide formed on the sample is shown in Figure 1. The layers discussed above (diffusion, inner and outer layers) are clearly seen. It is clear that the layers are fairly adherent, but that some porosity develops in the oxide layers. Some linear features are seen in the inner layer, possibly analogous to those seen in oxide layers formed on Zircaloy-4, and which undergo multiple oxide transitions [12]. The diffusion layer has variable apparent thickness, so the thickness measured during one scan (averaged over 2 microns laterally) will be specific to that location.
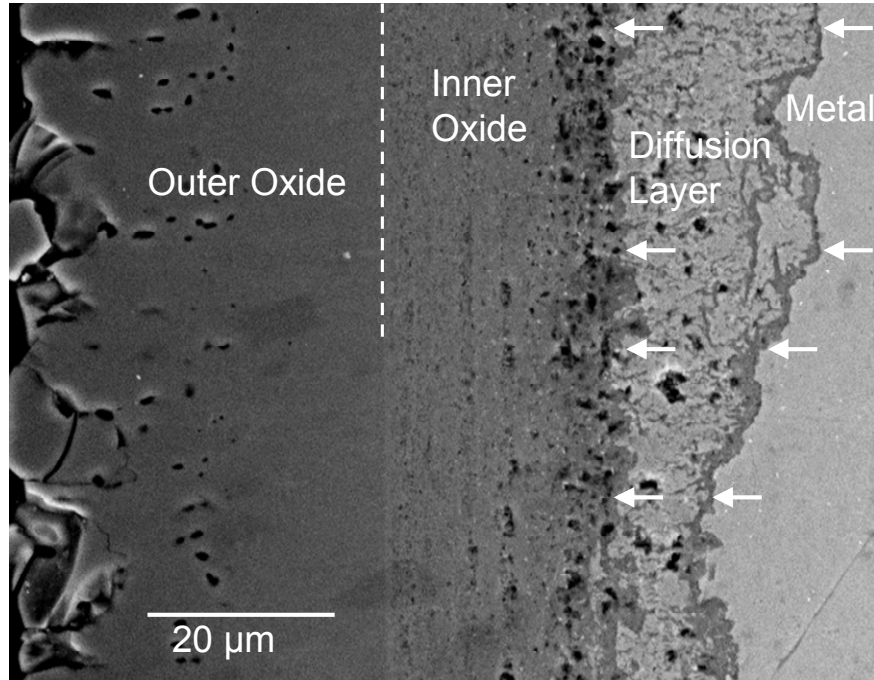
Figure 1: SEM image of different layers formed on 9Cr ODS steel during 677 h exposure to 600°C supercritical water.

Sample Preparation

The corroded coupons were cut using a diamond saw to reveal their cross-sections and then mounted in a molybdenum rod which slid into a 3 mm round brass tube, as done previously [12]. The sample configurations were held together with a copper-based epoxy, and samples sliced from the configuration such that their oxide cross-sections were still visible. These samples were then polished to a mirror finish with 1200 grit sandpaper followed by 1 micron colloidal silica and finally 0.1 micron diamond paste for examination in the synchrotron radiation facility.

Microbeam Synchrotron Radiation Diffraction and Fluorescence

In the beamline used at the Advanced Photon Source at Argonne National Laboratory, the incident beam can be focused to a 0.25 micron spot at an energy of 9.5 keV. The incidence angle used (14 degrees) created a footprint on the sample of 0.25 x 2 micron. The experimental geometry is shown in Figure 2. Fluorescence data (elemental analysis) and x-ray diffraction data (crystal phase and orientation) are gathered for each spot, and then the beam is moved to the next position and the process is repeated throughout the oxide layer. This data can be taken in 0.25 micron steps through the cross-section of the sample in order to obtain a "map" of the phases and elemental composition as it develops through the metal, into the diffusion layer, and finally in the oxide layers. In this case, because the oxide layer was thick, 1 micron steps were used.
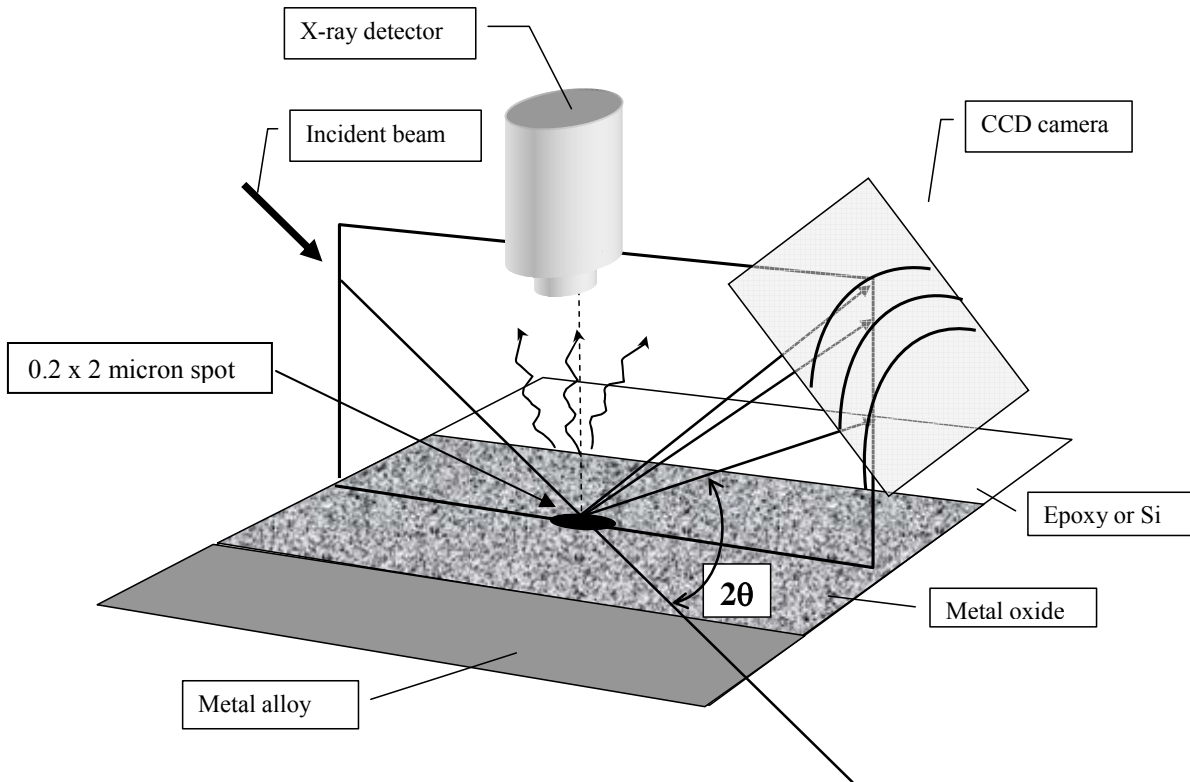
X-ray detector

Incident beam

CCD camera

0.2 x 2 micron spot

Epoxy or Si

2θ

Metal oxide

Metal alloy

Figure 2: Diffraction geometry at the microbeam synchrotron radiation diffraction and fluorescence beam line.

TEM

Transmission Electron Microscopy (TEM) samples were prepared using a Focused Ion Beam (FIB) at The Pennsylvania State University's Materials Research Institute Nanofabrication Facility. The model is a FEI Company Quanta 200 3D Dual Beam FIB. The FIB samples were prepared using a modified version of the lift-out method; in our case, the specimen was lifted from the bulk substrate first and then thinned to electron transparency. TEM images were obtained using a Philips 420 instrument operated at 120 keV.

3. Experimental Results

Transmission Electron Microscopy

Figure 3 illustrates the preliminary results for the TEM examination of the current sample, showing the overall oxide layer imaged in bright field. Two of the interfaces: the outer oxide-inner oxide (Fig 3 (a)), and the inner oxide-diffusion layer and diffusion layer-metal (Fig.3(b)) are shown. The outer layer consists of large oxide grains with a rectangular shape, while the inner oxide consists of smaller grains whose morphology is less well defined. Examinations of the chemistry by energy dispersive x-ray spectroscopy (not shown) in the region in the metal near the oxide show an elevated oxygen concentration in agreement with [11], and thus this layer is identified as the diffusion layer (also internal oxidation layer). The outer oxide, inner oxide and diffusion layer thicknesses were approximately 36, 20 and 20 μm, respectively.
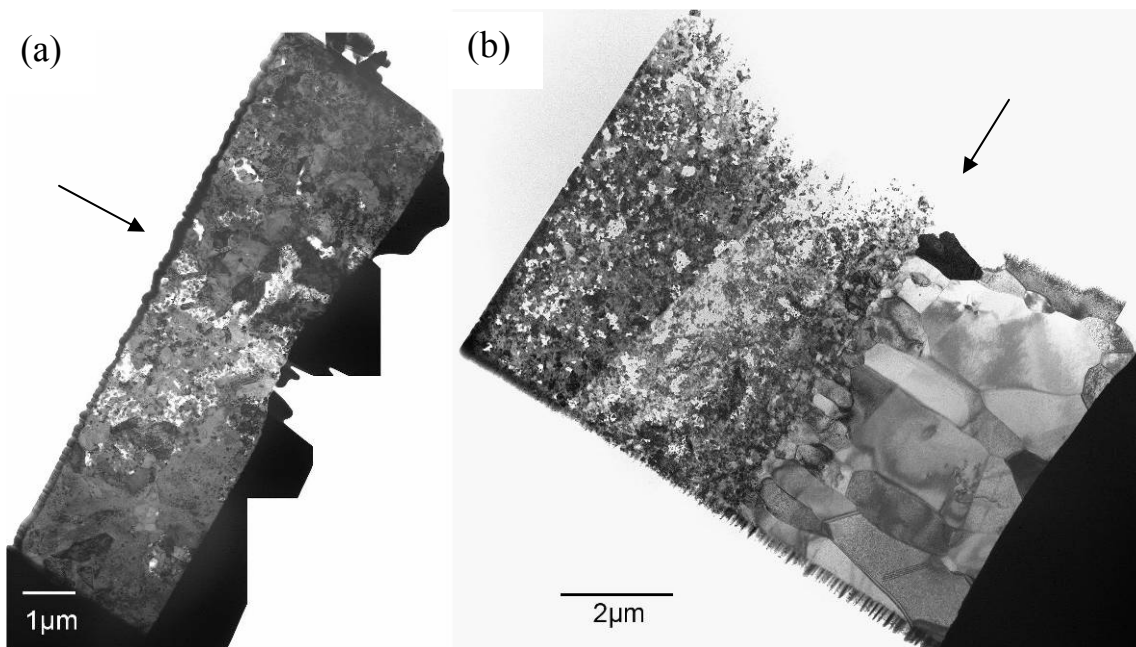
Figure 3: **TEM bright-field images for (a) the diffusion layer/inner oxide layer, and (b) inner layer/outer layer interfaces.**

The electron diffraction patterns taken from the outer layer can be indexed as the Fe_3O_4 fcc phase (powder diffraction file 19-629). The corresponding patterns from the inner oxide layer are more complex and exhibit evidence of ordered patterns similar to those observed by Chen et al.[11].

Microbeam synchrotron radiation fluorescence

Figure 4 shows the fluorescence data obtained during the scan of this oxide layer with the microbeam. Figure 4 (a) shows the profiles for the two major alloying elements, Fe and Cr, based on the integrated intensities of the K_α lines, as a function of location in the oxide layer. Figure 4(b) shows the intensities associated with W (L lines) and Ti ($K\alpha$ line). The four layers are quite visible and correspond well with the thicknesses measured by electron microscopy. It is clear that while the outer oxide contains no detectable Cr, the inner oxide layer is enriched in Cr relative to the base metal, with a somewhat lower Cr content in the diffusion layer.

This elemental distribution is consistent with the inner/outer oxide layer interface corresponding to the original sample surface, with the outer layer being formed by outward diffusion of Fe and the inner layer by inward diffusion of oxygen. The Fe used to form the outer layer would then come from both the diffusion layer and the inner oxide layers, leaving a relatively higher percentage of Cr in those layers. The higher amount of Cr is also consistent with the observation of Cr-rich phases in both the inner and diffusion layers, as discussed below.
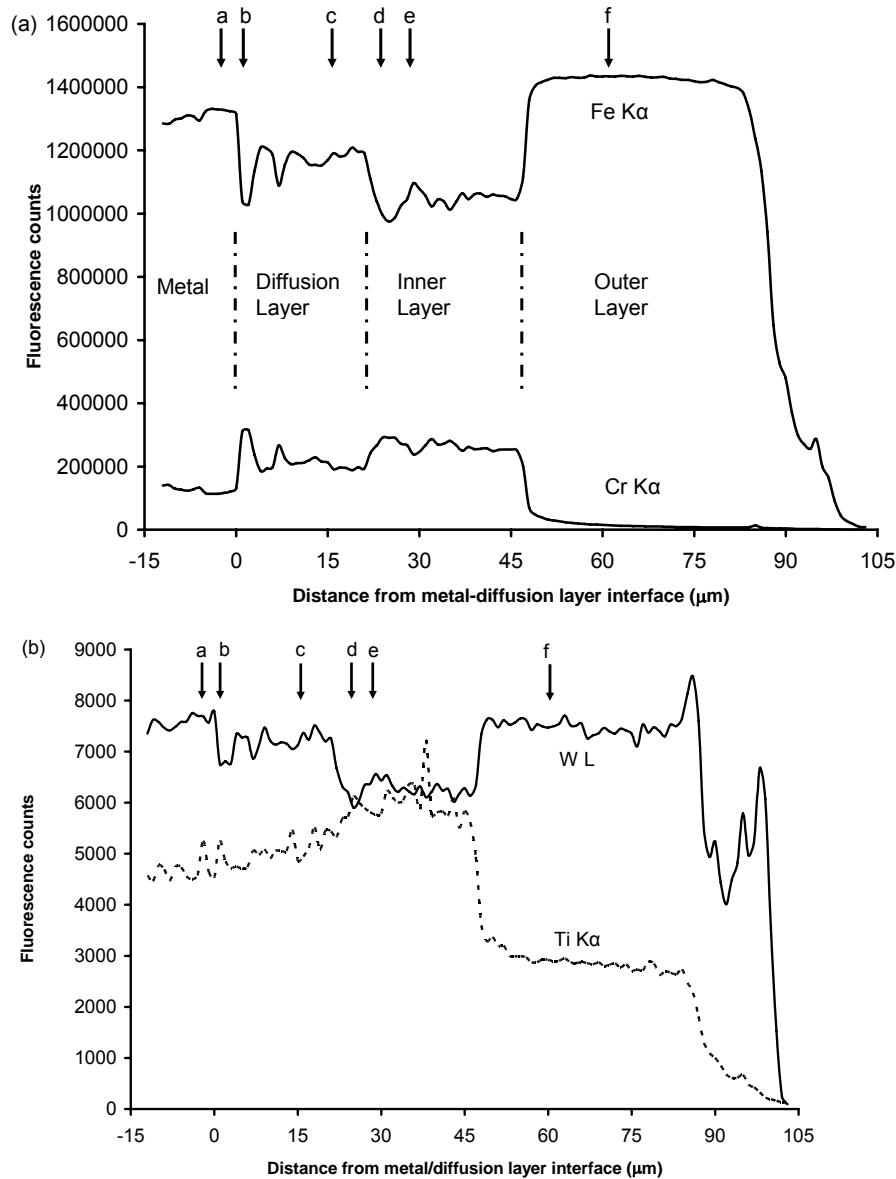
Figure 4: Fluorescence intensity as a function of distance from the metal-diffusion layer interface, forwith the lines indicated, obtained during microbeam scan of the oxide layer. (a) Fe K_α and Cr K_α. (b) W L and Ti K_α.

Figure 4(b) also shows that Ti is enriched in the inner layer relative to the outer layer but that there is some diffusion of Ti towards the outer layer. In contrast, W shows apparent enrichment in the outer layer. The W data should be taken with care as there are other elements that exhibit fluorescence lines in the same region as the W L line. An attempt was made to detect Y enrichment near the inner boundary of the inner layer since this would have been consistent with the proposed model of oxide protectiveness from yttrium oxide formation, but no increase in Y signal was detected. However the overall concentration of Y is quite low and it is possible that it is segregated laterally to the grain boundaries rather than to oxide interfaces [11]. It is also possible the steps were too coarse to allow detection of this Y rich zone.
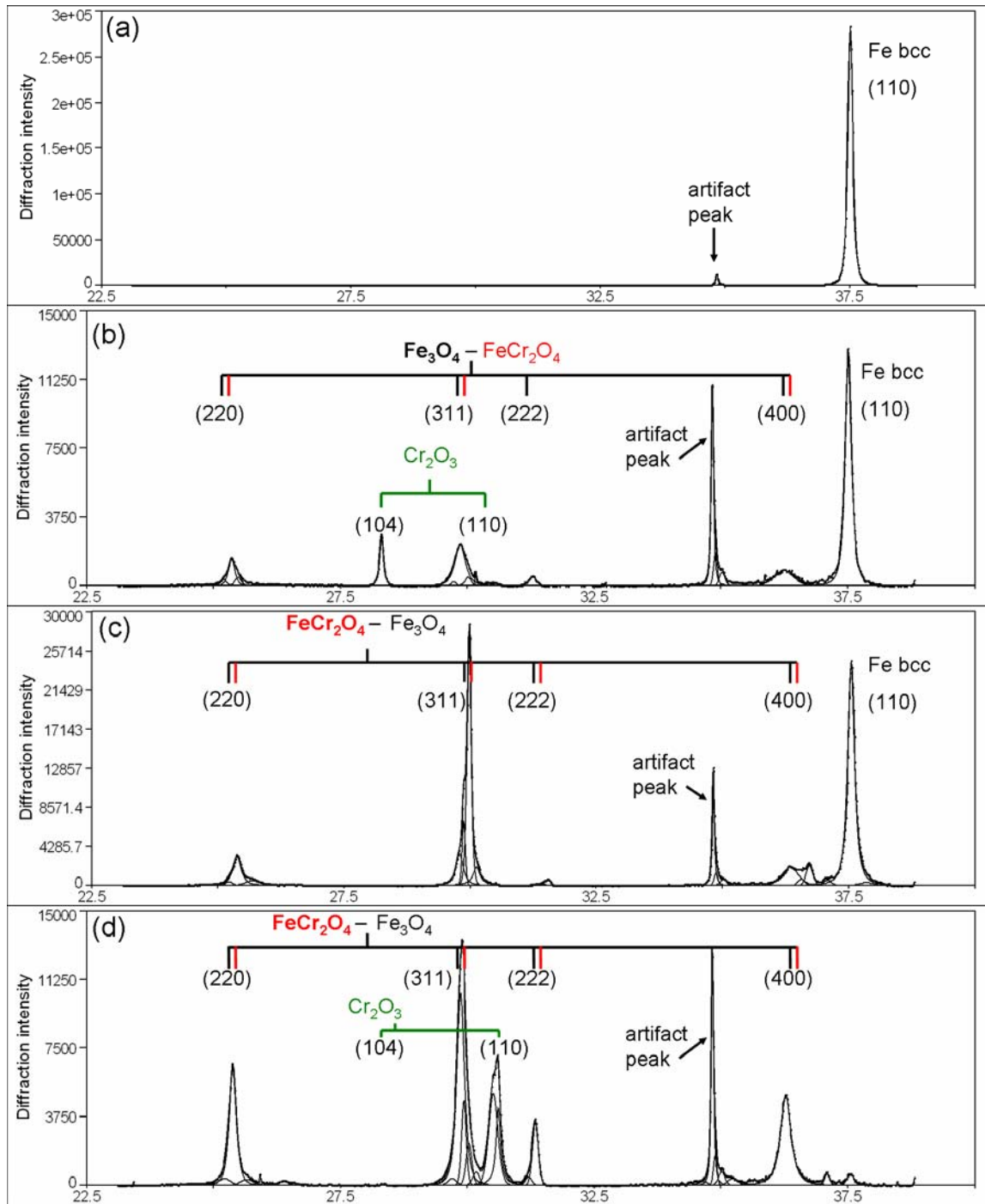
Figure 5: Diffracted intensity versus two-theta angle for various locations in the oxide sub-layers as indicated in Figure 4, showing curve fits and phase identification : (a) in the metal; (b) just inside the diffusion layer; (c) in the diffusion layer towards the oxide inner layer and (d) just inside the inner oxide layer.
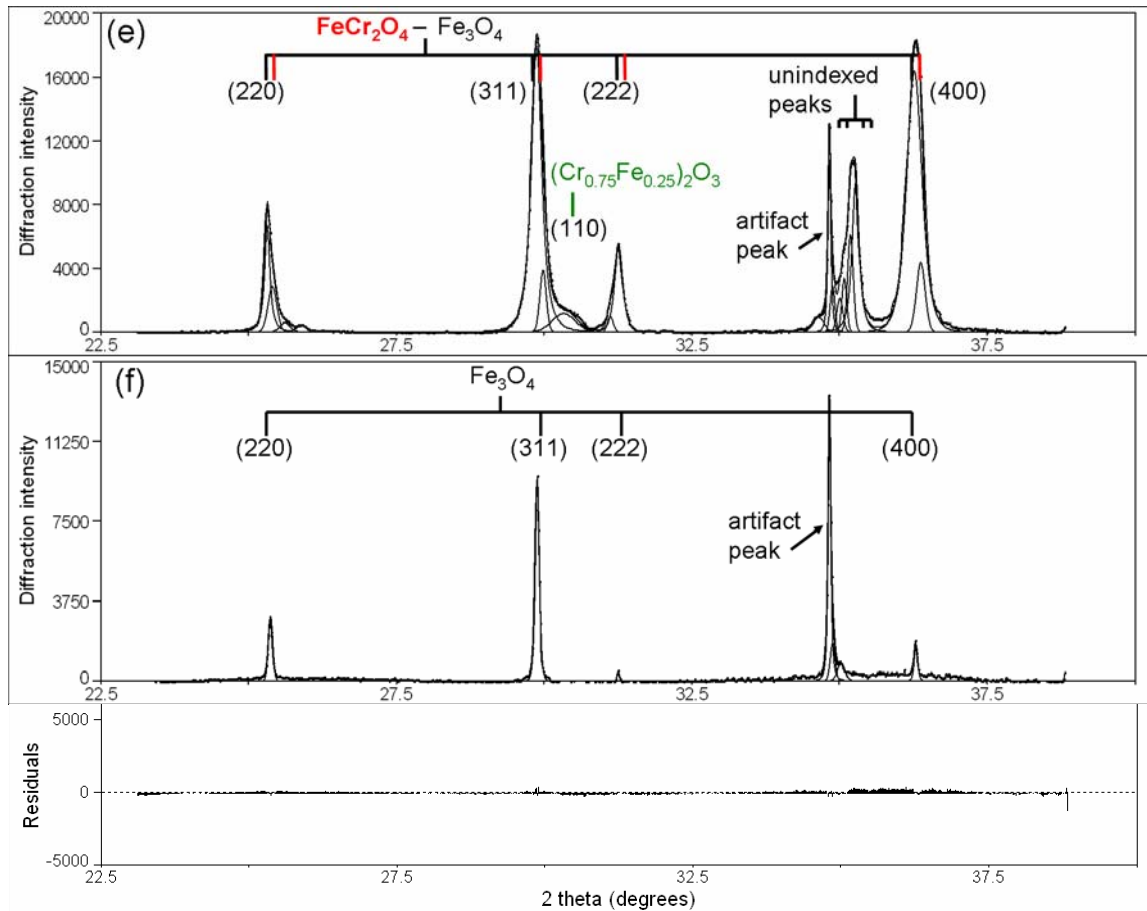
Figure 5 (cont.): Diffracted intensity versus two-theta angle for various locations in the oxide sub-layers as indicated in Figure 4, showing curve fits and phase identification : (e) near middle of inner layer; (f) in the outer layer; and (g) the residuals of the fit for the diffraction pattern in 5(f).

For each location in the oxide a complete diffracted intensity vs. two-theta angle was obtained. To analyze the microbeam diffraction data, the program Peak Fit version 4 is used. The peaks were fitted using a Pearson VII area peak shape. The centers of the peaks were then matched with peaks from likely phases for phase identification. The identification performed was precise within one hundredth of a degree two theta as shown below. This analysis was performed for all the diffraction patterns (>100) obtained from this oxide layer. Figure 5 shows six examples of the fitting from the locations indicated by the arrows in Figure 4. The fits obtained were very good; Figure 5 (g) shows the difference between fitted and measured intensities for the plot shown in Figure 5(f). The residuals are low and exhibit no preferential trend with two-theta angle.

Figure 5 (a) shows a diffraction pattern taken from position (a), in the bulk metal. In the metal only the 110 bcc peak shown is visible. Another peak at 34.8 degrees and marked "artifact", appears in every pattern and does not originate from the sample. In the diffusion layer, Figure 5(b), the same bcc Fe metal peak is visible, along with oxide peaks corresponding to Fe_3O_4,

the spinel phase FeCr$_2$O4 and to Cr$_2$O$_3$ oxide. This observation indicates that the diffusion layer is not a solid solution of oxygen in the metal but rather a mixture of bcc-Fe and oxide phase precipitates. It is also clear that the diffraction peaks associated with the Cr$_2$O$_3$ oxide phase are more prevalent in the portion of the diffusion layer closest to the metal, where a locally higher concentration of Cr also exists.

Signal from the bcc-Fe peak is not detected beyond the end of the diffusion layer, as expected. Most of the peaks observed in the inner oxide layer (Figures 5(d) and 5(e)) can be identified as belonging to either the spinel FeCr$_2$O$_4$ or fcc Fe$_3$O$_4$ structures. Although the two structures are quite similar, differing only slightly in lattice parameter, the peaks can be distinguished clearly in the synchrotron radiation diffraction experiments. For example the strongest peak (311) for the Fe$_3$O$_4$ phase is at 29.87 ° while the equivalent peak for the FeCr$_2$O$_4$ phase is at 29.94. The interface between the diffusion layer inner oxide, however, shows some additional peaks, some of which can be attributed to the Cr$_2$O$_3$ oxide phase, and four peaks around a theta angle of 35.2 degrees two-theta which currently do not have a positive identification, as shown in Figure 5(e). It is possible these peaks are associated with a phase formed with the minor elements present in the sample such as tungsten or titanium.

In comparing Figure 5(d) and Figure 5(e) taken from the inner layer, with Figure 5(f) from the outer layer it is clear that the broad peaks associated with a superposition of diffraction peaks from the spinel FeCr$_2$O$_4$ and the fcc Fe$_3$O$_4$ phase seen in the inner layer disappear such that only the Fe$_3$O$_4$ peaks are present in the outer layer. The Fe$_3$O$_4$ peaks in the outer layer show large intensity variations. These variations are attributed to the large grain size in the outer layer, which causes the diffraction condition to be satisfied only sporadically.
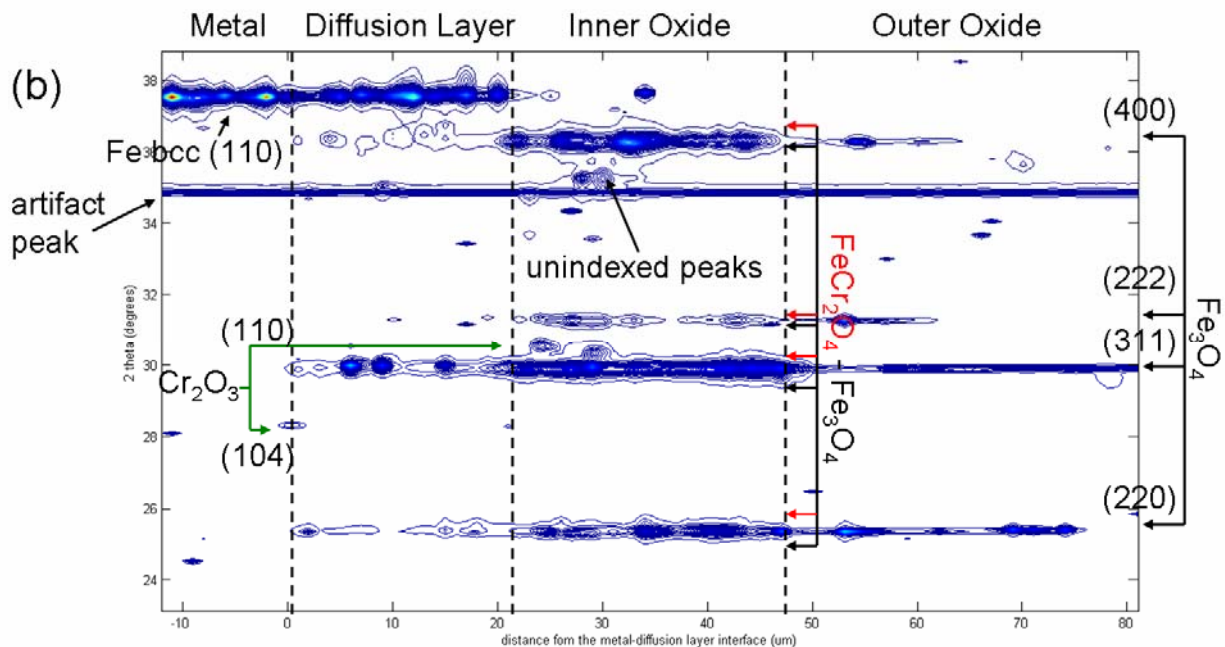

Figure 6: Two dimensional plot showing diffracted intensities versus location in the oxide and versus two-theta angle. The different oxide sub-layer regions are indicated and the peaks associated with each phase also shown.
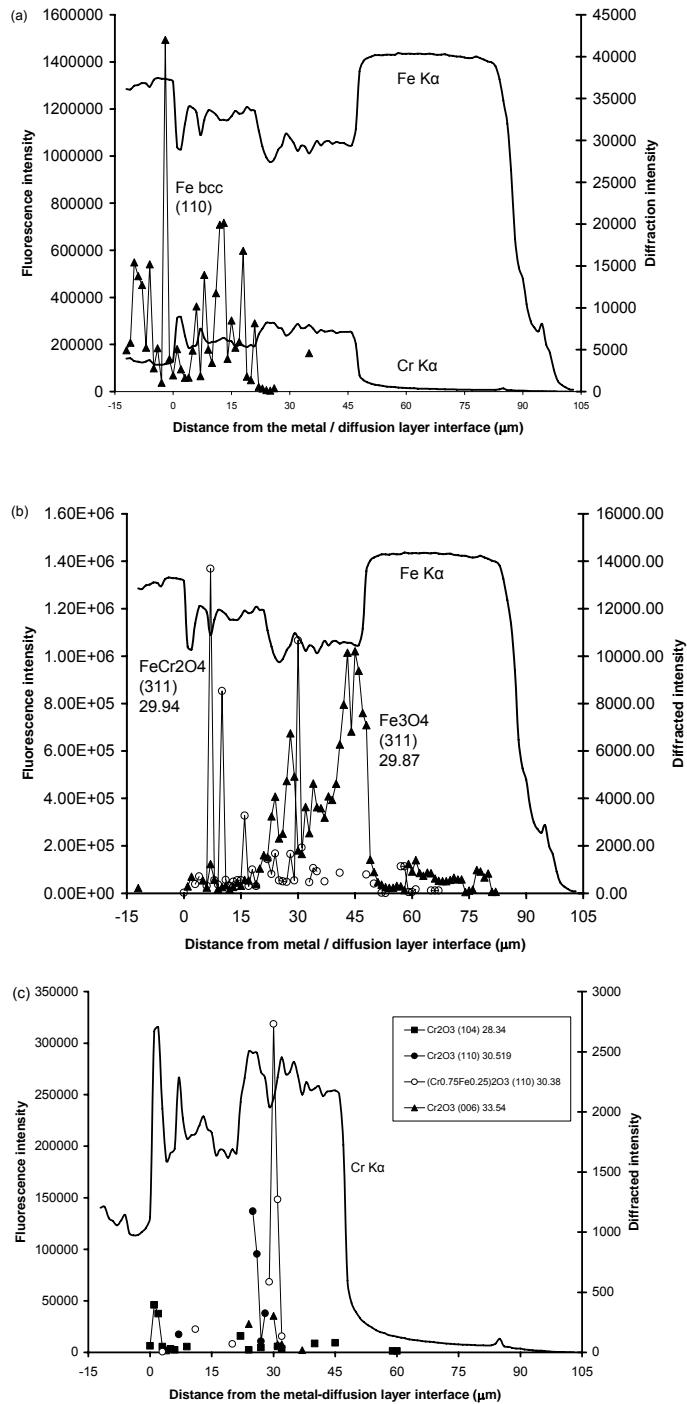
Figure 7: Diffracted peak intensities for the peaks indicated as a function of location in the oxide layer, as indicated by the fluorescence plots, for (a) bcc-Fe (b) spinel and Fe_3O_4, oxides and (c) Cr-rich phases.

The diffraction patterns obtained throughout the oxide layer are shown in Figure 6, in planar projection. The location of the layers is clearly seen, as well as the location of the phases

within the layers. The apparent "thinning" and shift of the doublet peaks belonging to the spinel $FeCr_2O_4$ (311) and the fcc Fe_3O_4 (311) mixture as they turn into only fcc Fe_3O_4 (311) in the outer layer is specially noticeable. These observations for the layers are summarized in Table 2, which lists the peaks identified and the corresponding two-theta location of the powder diffraction files. Thus in the inner layer both spinel and Fe_3O_4 phases coexist, while in the outer layer only Fe_3O_4 is present.

Table 2: Diffraction Peaks identified in the various oxide sub-layers from analysis of microbeam synchrotron radiation diffraction patterns.

Metal			Diffusion Layer						Inner oxide layer						Outer oxide layer		
			near metal and diffusion layer interface			near diffusion layer and inner oxide layer interface			near diffusion layer and inner oxide layer interface			near inner oxide and outer oxide layer					
Phase	observed peak	expected peak	Phase	observed peak	expected peak	Phase	observed peak	expected peak	Phase	observed peak	expected peak	Phase	observed peak	expected peak	Phase	observed peak	expected peak
Fe bcc	(110) 37.51	37.51	Fe bcc	(110) 37.51	37.51	Fe bcc	(110) 37.51	37.51									
			FeCr₂O₄	(311) 29.94	29.94	FeCr₂O₄	(311) 29.94	29.94	FeCr₂O₄	(311) 29.94	29.94	FeCr₂O₄	(311) 29.94	29.94			
										(220) 25.43	25.45		(220) 25.45	25.45			
										(222) 31.33	31.31		(222) 31.31	31.31			
										(400) 36.31	36.31		(400) 36.35	36.31			
			Fe₃O₄	(311) 29.87	29.87	Fe₃O₄	(311) 29.87	29.87	Fe₃O₄	(311) 29.87	29.87	Fe₃O₄	(311) 29.87	29.87	Fe₃O₄	(311) 29.87	29.87
			FeCr₂O₄ / Fe₃O₄	(220) 25.38	25.41	FeCr₂O₄ / Fe₃O₄	(220) 25.38	25.45 / 25.41		(220) 25.35	25.41		(220) 25.35	25.41		(220) 25.38	25.41
							(400) 36.26	36.31 / 36.22		(222) 31.25	31.23		(222) 31.25	31.23		(222) 31.25	31.23
										(400) 36.25	36.22		(400) 36.23	36.22		(400) 36.26	36.22
			Cr₂O₃	(104) 28.31	28.34				Cr₂O₃	(110) 30.51	30.51						
									Unknown peak	35.07 / 35.17 / 35.25 / 35.33							

The fitting of the diffraction patterns also allowed the determination of the intensity of the diffraction peaks as a function of location within the oxide scales. The diffracted intensities for the peaks from different phases (representing thus horizontal cuts through Fig.6) are shown in Figure 7 superimposed on the fluorescence profiles which indicate locations within the layers. It is clear from Figure 7 (b) that although the spinel $FeCr_2O_4$ and the fcc Fe_3O_4 are present throughout the inner layer, the spinel $FeCr_2O_4$ is the dominant phase in the inner part of the diffusion layer. These results are in qualitative agreement with those of Chen [11] who found similar phases in the corresponding layers. It is also clear that several peaks associated with Cr_2O_3 (and similar structures) are seen with higher intensities in the inner part of both the diffusion layer and the oxide inner layer, suggesting a possible role of this phase in the corrosion protection mechanism.

4. Conclusions

The microstructure of an oxide layer formed on a 9Cr ODS steel during exposure to 667 h in supercritical water was examined in detail using transmission electron microscopy and microbeam synchrotron radiation diffraction and fluorescence.

The main conclusions are:

1) The oxide layer shows three sub-layers. From the metal to the outer surface they are: an internal oxidation layer called the diffusion layer, an inner oxide layer and an outer oxide layer.

2) Transmission electron microscopy shows a well-defined interface between the inner and outer layers. Large grains are present in the outer layer and are identified as fcc-Fe_3O_4. The inner layer shows smaller grains.

3) Microbeam synchrotron radiation diffraction and fluorescence confirms the presence of Fe_3O_4 in the outer layer and shows a mixture of Fe_3O_4 and the spinel $FeCr_2O_4$ phase in the inner layer. The diffusion layer shows a mixture of bcc-Fe, Fe_3O_4 and of $FeCr_2O_4$ with the latter being prevalent near the diffusion layer-metal interface.

4) Additional peaks are seen in the inner parts of the inner oxide layer and of the diffusion layer, which are associated with the Cr_2O_3 phase and with an unidentified phase in the inner part of the inner oxide layer.

These results show that microbeam synchrotron radiation diffraction and fluorescence can yield detailed structural and phase information on oxide layers formed on ferritic-martensitic steels. The results are consistent with previous studies but reveal additional detail which it is hoped will lead to a better understanding of the corrosion mechanisms in these alloys.

Acknowledgments

References

[1]   T. R. Allen and D. C. Crawford, "Fuels and Materials Needs for Generation IV Nuclear Energy Systems," Proceedings of the ICAPP'03, Cordoba, Spain, (2003), American Nuclear Society, Paper no. 3237.

[2]   R. L. Klueh and D. R. Harries, High Chromium Ferritic and Martensitic Steels for Nuclear Applications. West Conshohocken, PA: ASTM, 2001.

[3]   T. Allen, R. L. Klueh, and S. Ukai, "Structural Materials for Transmutation Systems, Cladding and Duct Review," OECD NEA Report Number 5419, 2005.

[4]   S. Ohtuska, S. Ukai, M. Fujiwara, T. Kaito, and T. Narita, "Improvement of Creep Strength of 9Cr ODS martensitic Steel by Controlling Excess Oxygen and Titanium Concentrations," Materials Transactions, vol. 46, (2005), 1.

[5]   S. Ukai, S. Mizuta, T. Yoshitake, T. Okuda, M. Fujiwara, S. Hagi, and T. Kobayashi, "Tube Manufacturing and Characterization of Oxide Dispersion Strengthened Ferritic Steels," Journal of Nuclear Materials, vol. 283-287, (2000), 702.

[6]   M. K. Miller, D. T. Hoelzer, E. A. Kenik, and K. F. Russell, "Stability of Ferritic MA/ODS Alloys at High Temperatures," Intermetallics, vol. 13, (2005), 387.

[7]   J. Stringer, "The Reactive Element Effect in High-temperature Corrosion," <u>Materials Science and Engineering, A</u>, vol. 120, (1989), 129.

[8]   P. Y. Hou and J. Stringer, "The Effect of Reactive Element Addition on the Selective Oxidation, Growth and Adhesion of Chromia Scales," <u>Materials Science and Engineering</u>, vol. A202, (1995), 1.

[9]   C. M. Cotell, G. J. Yurek, R. J. Hussey, D. F. Mitchell, and M. J. Graham, "The Influence of Grain-boundary Segregation of Y in Cr_2O_3 on the Oxidation of Cr Metal," <u>Oxidation of Metals</u>, vol. 34, (1990), 173.

[10]   T. A. Ramanarayanan, R. Ayer, R. Petkovic-Luton, and D. P. Leta, "The Influence of Yttrium on Oxide Scale Growth and Adherence," <u>Oxidation of Metals</u>, vol. 29, (1988), 445.

[11]   Y. Chen, K. Sridharan, T. R. Allen, and S. Ukai, "Microstructural Examination of Oxide layers Formed on an Oxide Dispersion Strengthened Ferritic Steel Exposed to Supercritical Water," <u>Journal of Nuclear Materials</u>, vol. 359, (2006), 50.

[12]   A. Yilmazbayhan, A. T. Motta, R. J. Comstock, G. P. Sabol, B. Lai, and Z. Cai, "Structure of Zirconium Alloy Oxides formed in Pure Water Studied with Synchrotron radiation and Optical microscopy: Relation to Corrosion Rate," <u>Journal of Nuclear Materials</u>, vol. 324, (2004), 6-22.

[13]   A. T. Motta, A. Yilmazbayhan, R. J. Comstock, J. Partezana, G. P. Sabol, Z. Cai, and B. Lai, "Microstructure and Growth Mechanism of Oxide Layers Formed in Zr Alloys Studied with Micro Beam Synchrotron Radiation," <u>Journal of ASTM International</u>, vol. 2, (2005), Paper # JAI 12375.

[14]   Q. Peng, E. Gartner, J. T. Busby, A. T. Motta, and G. S. Was, "Corrosion Behavior of Model Zirconium Alloys in Deaerated Supercritical Water at $500^{o}C$," <u>Corrosion</u>, vol. 63, (2007), 577-590.

[15]   A. Motta, A. Yilmazbayhan, M. Gomes da Silva, R. J. Comstock, G. Was, J. Busby, E. Gartner, Q. Peng, Y. H. Jeong, and J. Y. Park, "Zirconium Alloys for Supercritical Water Reactor Applications: Challenges and Possibilities," <u>Journal of Nuclear Materials</u>, in print, (2007).

[16]   K. Sridharan, A. Zillmer, J. R. Licht, T. R. Allen, M. H. Anderson, and L. Tan, "Corrosion Behavior of Candidate Alloys for Supercritical Water Reactors," Proceedings of ICAPP 04, Pittsburgh, PA, (2004), 537.